RESEARCH ARTICLE | FEBRUARY 25 2025

Particle swarm optimization of 1D isochoric compression designs for fast ignition

M. Brönner ✉ ; S. Atzeni ; D. Callahan ; J. Gaffney ; P. Gibbon ; L. C. Jarrott ; A. Mateo ; L. Savino ; N. Schott ; W. Theobald ; M. Roth

Phys. Plasmas 32, 022710 (2025)
https://doi.org/10.1063/5.0244435

Physics of Plasmas ARTICLE pubs.aip.org/aip/pop

Particle swarm optimization of 1D isochoric compression designs for fast ignition

Cite as: Phys. Plasmas **32**, 022710 (2025); doi: 10.1063/5.0244435
Submitted: 18 October 2024 · Accepted: 31 January 2025 ·
Published Online: 25 February 2025

M. Brönner,[1,2,a)] S. Atzeni,[1] D. Callahan,[3] J. Gaffney,[3] P. Gibbon,[1,4] L. C. Jarrott,[3] A. Mateo,[1,5] L. Savino,[6] N. Schott,[1,2] W. Theobald,[1,7] and M. Roth[1,2]

AFFILIATIONS

[1] Focused Energy GmbH, 64293 Darmstadt, Germany
[2] Department of Physics, Institute for Nuclear Physics, Laser- and Plasmaphysics, Technische Universität Darmstadt, 64289 Darmstadt, Germany
[3] Focused Energy Inc., Austin, Texas 78758, USA
[4] Forschungszentrum Jülich, Juelich Supercomputing Centre, 52428 Jülich, Germany
[5] ETSI Aeronáutica y del Espacio, Universidad Politécnica de Madrid, 28040 Madrid, Spain
[6] Dipartimento SBAI, Universitá di Roma 'La Sapienza', 00161 Roma, Italy
[7] Department of Mechanical Engineering, University of Rochester, 14611 Rochester, New York, USA

[a)] Author to whom correspondence should be addressed: matthias.broenner@focused-energy.world

ABSTRACT

A method to study isochoric compression to mass densities relevant for direct-drive fast ignition schemes is presented. The method is based on the combination of one-dimensional radiation-hydrodynamic simulations using the code MULTI-IFE [Ramis and Meyer-ter Vehn, Comput. Phys. Commun. **203**, 226 (2016)] and a particle swarm optimization technique [Kennedy and Eberhart, in Proceedings of ICNN'95 - International Conference on Neural Networks (IEEE, Perth, WA, Australia, 1995), Vol. 4, pp. 1942–1948]. The compression of the fuel is optimized through variations of the incident temporal laser power profiles. Uniform mass density profiles are achieved by using appropriate objective functions that allow comparisons between the fuel assemblies obtained from simulations. Several objective functions were created and evaluated on their merits to yield isochoric compression assembly. Ultimately, such a profile is presented in conjunction with the technique to achieve it. A useful objective function is calculating the deviation of the simulated mass density profile from the ideal uniform mass density profile over a volume of the compressed target up to the radial position of the outgoing shock wave.

I. INTRODUCTION

The major break-through in laser-driven inertial confinement fusion (ICF) at the National Ignition Facility (NIF) at the Lawrence Livermore National Laboratory[3–6] of fusion energy gain exceeding unity presents a big milestone on the pathway to inertial fusion energy (IFE). The scheme employed by the NIF, often referred to as indirect drive central hotspot ignition, accelerates a spherical shell of deuterium tritium (DT) fuel to high velocities ($\sim 400\,\mathrm{km\,s^{-1}}$). At stagnation, a high density shell of fuel surrounds a low density hotspot that is heated by pdV (pressure times change in volume) work. The configuration is approximately isobaric where the low density, high temperature hotspot is in near pressure balance with the high density, cold fuel shell.[7] Fusion reactions occur in the hotspot and the resulting alpha particles deposit their energy in the hotspot. The alpha particle heating overcomes radiation and thermal heat conduction losses. A thermal instability occurs resulting in a burn wave that propagates through the fuel shell. The reaction ceases when the capsule, which is only held together by its own inertia, explodes. Depositing enough energy into the hotspot, while also compressing the fuel to high densities, places strong constraints on the implosion.[8]

A potential pathway to high gain designs with laser energies up to 2 MJ might be achieved by fast ignition schemes.[9,10] In these schemes the stages of fuel compression and the generation of a hotspot required for ignition are partly separated. The fuel is first compressed by imploding a capsule, as in conventional ICF schemes, but at a lower implosion velocity (typically lower than $300\,\mathrm{km\,s^{-1}}$ instead of $400\,\mathrm{km\,s^{-1}}$). This reduces the risks associated with hydrodynamic instabilities and allows assembling a larger fuel mass, supporting a higher gain, for a given implosion kinetic energy. The hotspot needed for ignition is then created in the compressed assembly by an external source, instead of by hydrodynamic flow. For the ignitor there have been proposals to use relativistic electron beams,[9] multi-MeV proton,[11] or light ion beams,[12,13] accelerated by ultra-intense laser beams. Regardless of the ignitor choice, the required total particle beam energy E_{b} is a decreasing function of the fuel density ρ ($E_{\mathrm{b}} \propto \rho^{-m}$, with $m = 1.3 - 1.85$[14]) and the particle range has to be shorter than $1\,\mathrm{g/cm^2}$. The optimal beam radius r_{b} and pulse duration t_{b} are about inversely proportional to the density ($r_{\mathrm{b}} \propto \rho^{-1}$; $t_{\mathrm{b}} \propto \rho^{-1}$). Considering beam focusing limitations, typical foreseen parameters are $\rho = 300 - 400\,\mathrm{g/cm^3}$, $r_{\mathrm{b}} = 15\text{–}20\,\mu\mathrm{m}$, and $t_{\mathrm{b}} = 10\text{–}20\,\mathrm{ps}$.[15,16] Most fast ignition schemes, using either fast electrons or fast ions as an ignitor beam, utilize a cone inserted in the shell to keep a clear channel for the ultra-intense beam which allows efficient production of the ignitor and minimizes the distance to the compressed fuel.[10,14,17]

The status and perspectives of electron fast ignition and proton fast ignition were reviewed, respectively, in Refs. 18 and 17 and 13 and 19. More recent work on electron fast ignition is reported in Refs. 20 and 21, and for protons in Refs. 22 and 23, and ions in Ref. 24.

The central hotspot that usually forms during the implosion is not required for ignition. Therefore, a constant density profile (isochoric) with a negligible central hotspot is preferred, which provides advantages in fast ignition schemes for the ignition and burn phase. It was shown that the ignition energy depends on the shape of the compressed fuel with an ideal isochoric density profile providing the lowest required ignition energy[13,25,26] highlighting the importance of the assembled density profile.

One option to ignite the fuel is by a short pulse laser generated proton beam in the proton fast ignition (pFI) scheme.[11,19] Target designs for pFI commonly utilize a cone that shields the proton acceleration target from the pressure of the implosion and is used to allow access to the compressed fuel core for the proton beam. Isochoric fuel assemblies minimize the fuel pressure close to the cone tip at stagnation, which might lead to a decrease in the stand-off distance between the compressed fuel and the cone tip. This reduces the amount of proton energy necessary for ignition by minimizing proton losses.

The design space for the implosion is vast. The target can consist of different layers with varying thicknesses, while the driver of the implosion can be composed of pickets, ramps, steps, or combinations thereof. A metric that judges the implosion is related to many system specific parameters. Particularly in pFI, the optimal compressed density that minimizes proton beam energies is related to the achievable proton focus size.[14,16] The optimal shape from a one-dimensional design might not be the optimal shape of a three-dimensional implosion once the cone breaks up the symmetry.[27] The required proton beam energy also varies with different shapes of the compressed fuel.[13,25,26] During the implosion the growth of Rayleigh-Taylor instabilities could breakup the shell, which might constrain the implosion designs to a range of adiabats (defined as the ration of the plasma pressure in the fuel shell and the Fermi-degenerate pressure at the shell density) and in-flight shell thicknesses.[28] All these factors and many more contribute to a challenging optimization problem where iterations with different codes, i.e., multidimensional radiation-hydrodynamic simulations or particle-in-cell simulations are of utmost importance. Accordingly, the used optimization technique has to be robust to deal with multi modal problems and not converge too quickly on a local optimum. A flexible technique is required where the objective functions, i.e., the metric chosen for optimization, can be adjusted with complex combinations of output parameters.

Particle swarm optimization (PSO) is a gradient-less global optimization method that combines all these useful features.[2] Since the optimization cycles query the objective function in batches, which is quite common in optimizations, we can run multiple simulations in parallel to speed up the optimization considerably. We combined PSO with 1D radiation-hydrodynamic simulations with the code MULTI-IFE.[1] In this paper, we present design studies that tune temporal laser pulses in order to obtain an isochoric fuel profile in a direct-drive implosion. As a starting point, we use the self-similar isochoric implosion design by Clark and Tabak.[29] We show a technique that is able to obtain laser pulse shapes to compress the fusion fuel to high density isochoric fuel profiles.

In Sec. II, we explain the particle swarm optimization technique. The setup of the simulations is discussed in Sec. III. The results are presented and discussed in Sec. IV. Finally, a conclusion is drawn in Sec. V.

II. PARTICLE-SWARM-OPTIMIZATION

Particle swarm optimization (PSO) is an optimization technique that is inspired by the behavior of groups of animals.[2] A population of so-called agents can find the global optimum of a nonlinear function efficiently by sharing some information about promising locations. The technique operates by initializing a swarm of agents, also known as particles, in a parameter space, we call input space. In our case, the coordinates in the input space describe a temporal laser power profile and each dimension can control the power at a certain point in time. The particles move around in this space and search for the optimum. This is achieved by giving each particle a velocity in the input space that is updated in each step and utilizes the knowledge of the previous steps. A set of hyperparameters that can be tuned to adjust the behavior of the swarm determines this update.

Every optimization cycle i is treated as a unity time step where the position x of a particle j is modified by its velocity v

$$x_{j,i+1} = x_{j,i} + v_{j,i+1}. \tag{1}$$

Both the position and the velocity have the same number of dimensions as the input space. The velocity of the optimization cycle $i+1$ for particle j is modified by

$$v_{j,i+1} = \overbrace{h_1 \cdot v_{j,i}}^{\text{①}} + \overbrace{r_1 \cdot h_2 \cdot (B_{\mathrm{S}} - x_{j,i})}^{\text{②}} + \overbrace{r_2 \cdot h_3 \cdot (B_j - x_{j,i})}^{\text{③}}. \tag{2}$$

This update to the velocity $v_{j,i+1}$ is executed before the position update and can be adjusted by modifying the hyperparameters $h_{\{1,2,3\}}$. The first term ① of Eq. (2) determines the decay of the velocity with a hyperparameter h_1. This controls the property of the swarm tending to overshoot on found optima and is sometimes called the inertia term. The second term ② of Eq. (2) is a "pull" toward the best found point by the whole swarm B_{S}. The term is proportional to the distance of the particle to the point and multiplied by a random number between zero and one called r_1. This corresponds to the utilization of "public knowledge" and increasing the associated hyperparameter h_2 causes the swarm to converge faster on a region of the input space. Finally, every particle experiences a similar pull term ③ to their respective best found points B_j. This is also proportional to the distance to the point and multiplied by a random number r_2 between zero and one. Increasing the hyperparameter h_3 results in the particles searching their respective neighborhood and converging slower, which can prevent getting stuck in local optima. The random numbers in the pull terms are necessary for particles to not converge on points between optima.[2,30]

An advantage of this optimization method is that the rules for the movement of the particles are simple which provides good access to the dynamics of the optimization. Since the particles query the objective function in every optimization cycle once and at the same time, the call to the objective function can make use of parallel processing. This speeds up the optimization considerably where the total run time of the optimization is mostly attributed to the simulations. In our studies, we also found that the dynamics of the swarm can work well in a larger dimensional input space of 18 dimensions while dealing with a multi-modal problem where multiple local optima are present. It is, however, unknown if the optima, we observed are the global optima or only local optima. This is an issue that persists to the most recent reviews of the technique.[31] Since the whole dynamics of the swarm is controlled by the hyper parameters their choice is crucial to the robustness of the method but is problem dependent.[31]

We started our optimizations with hyperparameters $h_1 = 0.7298$, and $h_2 = h_3 = 1.49618$ from the constricted particle swarm.[30,32] Since the swarm did not show enough convergence and needed too many cycles, we reduced h_3 to a value of 1, which yielded better results. We use 50 optimization cycles with 400 particles unless stated otherwise, which takes of the order of a day with 80 parallel processes on a modern CPU. We search for the maximum of our objective functions, of which we call the different iterations O_n.

III. SIMULATION SETUP

To employ the optimization scheme, we need to map the dimensions of the particle positions to laser power pulse shapes and simulate the implosions. We couple the PSO to radiation-hydrodynamics simulations using the code MULTI-IFE.[1] MULTI-IFE uses a Lagrangian scheme with a two temperature plasma model, thermal diffusion, multi-group radiation transport, and inverse Bremsstrahlung laser absorption coupled to a 3D ray-tracing algorithm. Matter properties are described by tabulated equations of state (EOS), requiring the internal energy as a state variable. To run MULTI-IFE with the SESAME[33] EOS, we modified the code to run with temperature instead of energy as a state variable. To prevent unphysical expansion of the materials at low temperatures, we implemented a quiet start option similar to the one described by Haines *et al.*[34] We disable hydrodynamics motion as long as a cell has not reached a threshold temperature of the order of 10^{-3}eV before. To validate the update, we performed a limited number of tests with results from simulations with the code DUED[35,36] using ACP EOS[37] and found good agreement. We also modified the output routine to work faster and easier with our Python code of the PSO. We run multiple simulations at the same time using multiprocessing pools in Python.

The target in all presented simulations is based on the design by Clark and Tabak,[29] which is shown in Fig. 1.

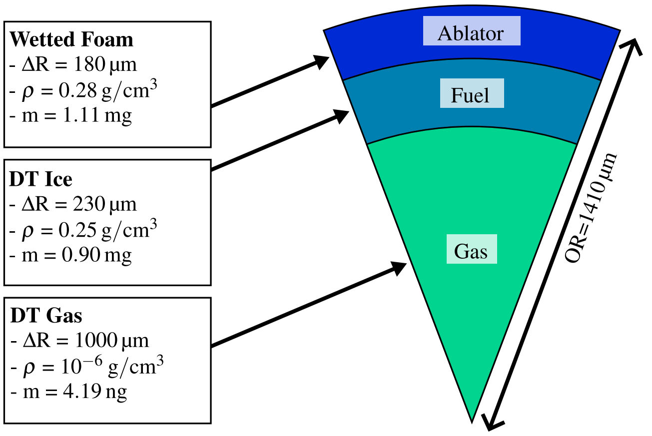

FIG. 1. Schematic of the used target reproduced from Clark and Tabak.[29] The inner part of the spherical target consists of low density DT gas that is surrounded by a solid DT ice shell. The outer layer is made out of DT wetted plastic foam as an ablator for the implosion. The outer radius OR, thickness ΔR, initial mass density ρ, and total mass m of the layers are included.

We use the SESAME EOS tables in combination with ionization and opacity tables generated by SNOPMIX (SNOP[38] with modifications by S. Atzeni). Since we do not have access to a wetted foam equation of state, we used a scaled version of the DT table to the appropriate average charge and mass number. SNOPMIX allowed the use of the appropriate tables for the wetted foam mixture. The number ratio of the wetted foam consists of 12% CH and 88% DT. The 1000 μm thick DT gas at the center is described by 10 cells of the same thickness. We use 400 cells for the 230μm of DT ice and 300 cells for the 180 μm of wetted foam ablator. The cells in the wetted foam ablator are of uniform thickness while the ice cells utilize varying cell thicknesses in two layers with the same number of cells. In the respective layers the thickness of a cell is calculated by multiplying the thickness of the previous cell with the multiplier of the respective layer. We choose the multipliers in the layers such that the ice cells at the layer interfaces match the multiplication of the cell density with the thickness of the neighboring cell.

The laser power over time is created by taking the original direct-drive pulse from Clark and Tabak and applying changes to it. The laser wavelength is 351 nm. We select 15 time-power points and modify their power by a factor between 0.5 and 1.5 where each of these modifications represents one dimension of the particle swarm input space. The initial parts of the pulse are not modified in order to set the adiabat with the strength of the first shock where the first point modified is at 11.4 ns. We add 19 log-linear interpolated points between two respective modified time-power points. In the MULTI simulation, we use linear interpolation. An illustration of the changes in the laser pulse shape is shown in Fig. 2. We stretch the time axis of the pulse by a factor between 0.9 and 1.1 which amounts to another input space dimension. Finally, the pulse is normalized to an energy of 485 kJ by applying a power multiplier on the entire pulse. Although this changes the initial parts of the pulse as well, this does not significantly affect the adiabat.

The laser focal spot size is modeled as a super-Gaussian with an exponent of 16. The beam radius defined by the power falling to $1/e^2$ of the peak power was varied between 30% to 50% of the targets initial outer target radius, which is also controlled by an input parameter. A small focal spot size achieves a good energy coupling to the capsule in most cases although the final design will need a larger focal spot size to achieve a symmetric implosion.

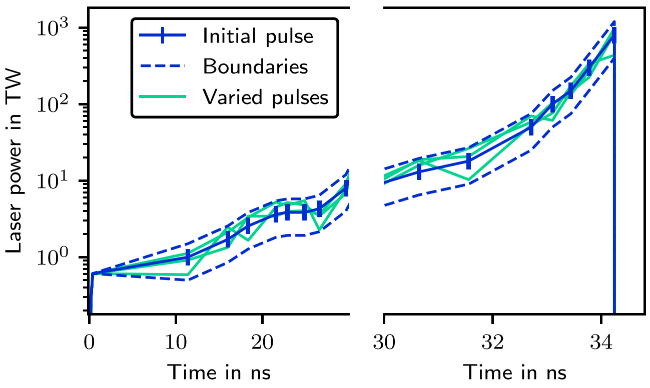

FIG. 2. The initial laser pulse of the incident power over time is shown as a blue curve. The blue vertical lines mark the times where the power is modified by multipliers. The upper and lower boundaries, obtained by choosing the maximum or minimum multipliers, show the curves before modifications to the power axis are done. Three random example pulses are drawn in green. At 30 ns we zoom the time axis in this illustration for better visibility of the ramp. After the application of the multipliers the whole pulse is also stretched in time and normalized to the same energy for all pulses by applying a power multiplier.

IV. RESULTS

Our goal is to find a technique for the PSO, which helps to find isochoric fuel profiles relevant for pFI. To do so, we must define the objective function that is used to evaluate each implosion.

For a given target with a given fuel mass, the thermonuclear yield depends on the burn fraction if ignited. The burn fraction Φ can be approximated as a monotonically increasing function of the areal density[7]

$$\Phi = \frac{\rho R}{\rho R + H_B}, \text{ with} \tag{3}$$

$$\rho R = \sum_n \rho_n d_n. \tag{4}$$

The sum is calculated over all DT fuel cells, ρ_n is the mass density in a cell, d_n the radial thickness of a cell with number n, and H_B is the burn parameter. Therefore, by maximizing the areal density, we can obtain the highest possible yield of a given target. We tested this first objective function

$$O_1 = \rho R, \tag{5}$$

with the particle swarm on our test set, where we take the areal density at the time it is maximized in a simulation. The optimized fuel profile in Fig. 3 shows a large density spike (>1500 g/cm^3) at a small radial position (∼5 μm). The pulse was achievable these very high densities by careful timing of multiple shocks onto a low adiabat inner shell and utilizing a very high ablation pressure of the order of 1Gbar for the last shock. While this optimization results in a very high ρR, the densities are far from optimal for pFI, where the required ignition energies are minimized by densities of the order of 300 to 450 g/cm^3 depending on the achievable proton deposition region.[14,39] We require a different objective function in order to achieve an isochoric fuel profile with a high areal density that simultaneously minimizes the ignition energy.

In our next attempt, we minimize the deviation from a constant mass density profile. The metric we use to measure this is the cell mass weighted root mean square-error

$$\text{RMSE}(\rho_T, N) = \sqrt{\frac{\sum_{n=1}^{N} (\rho_n - \rho_T)^2 \cdot m_n}{\sum_n m_n}}, \tag{6}$$

where ρ_n is the mass density and m_n the mass of cell number n. ρ_T is the mass density we want to achieve with the compressed fuel. We mass average the root mean squared error of all fuel cells, where N_{DT} is the cell number of the outermost DT cell, and choose $\rho_T = 300\,\text{g/cm}^3$ for the objective function

$$O_2 = -\text{RMSE}(300\,\text{g/cm}^3, N_{DT}), \tag{7}$$

where the value of the objective function is evaluated at the time it is maximized in the simulation. In the optimized density profile in Fig. 4 it can be seen that at the time of minimum error, the outgoing shock is just passing the fuel ablator interface. Around the center, the profile approaches the requested 300 g/cm^3, but only for a small fraction of the target mass. Thus, we deemed the objective function not appropriate for our goal. We tested small tweaks on the metric, like a cell thickness average instead of a mass average, but the time of minimum error

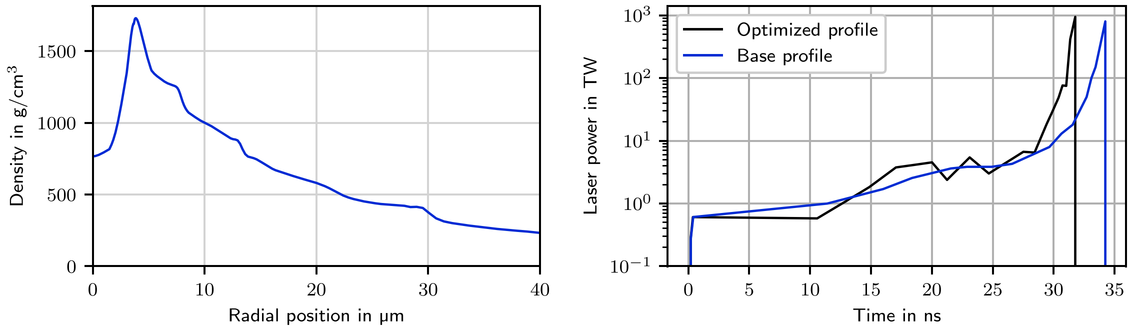

(I) Mass density profile.

(II) Temporal laser profile.

FIG. 3. Mass density profile (I) achieved by optimizing O_1 at the time of peak areal density (3.66 g/cm^2). In (II) we show the temporal laser power profile used together with the base profile from Fig. 2.

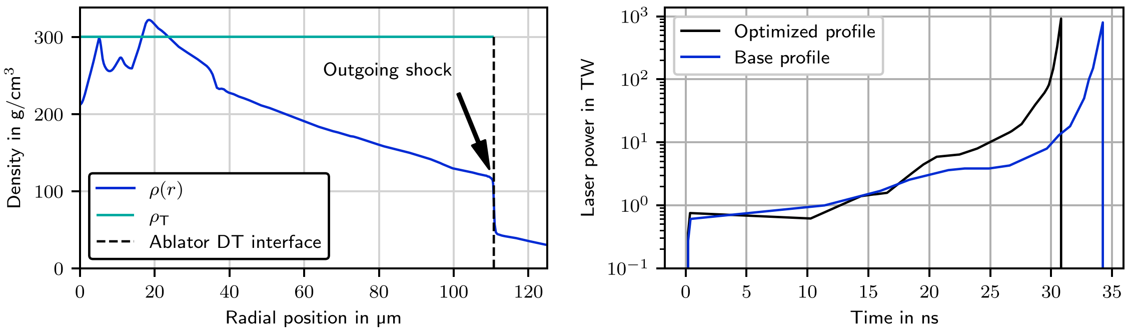

(I) Mass density profile.

(II) Temporal laser profile.

FIG. 4. Mass density profile achieved by optimizing O_2 in (I). The blue curve is the profile at the time the RMSE is minimized. The vertical dashed green line shows the position of the fuel ablator interface at this time step and the horizontal green line the targeted density of 300 g/cm^3. The implosion achieved a peak areal density of 2.29 g/cm^3. The used laser power over time can be found in the plot in (II) in conjunction with the base profile from Fig. 2.

always coincided with the outgoing shock leaving the fuel. We concluded that we need a different way of limiting the outer radius for the calculation of the root mean squared error.

In the next attempt, we used a commonly used shell metric in ICF implosions.[40] The shell in this metric is limited by the density falling below the maximum density over Eulers number. The first cell to higher radii of the maximum density fulfilling that condition is called N_{OS}. We use this to define the outer boundary of the integration volume while we keep the inner boundary always at the center. In addition to this change, we also compute a mass average density $\bar{\rho}$ of the imploded shell. Instead of only minimizing the density error, we now reward higher average densities in

$$O_3 = -\mathrm{RMSE}(\bar{\rho}, N_{\mathrm{OS}} - 1) + w_{\mathrm{d}} \cdot \bar{\rho}, \tag{8}$$

where the maximum value of O_3 in a given simulation is taken. The ratio between the two terms is tuned by a new hyperparameter called the density weight w_{d}. We performed three optimizations varying the density weight from 0.05 to 0.15.

The results shown in Fig. 5 yielded a close to linear relationship between average density and density weight. All three optimized density profiles show a density spike close to a radius of zero. Except for that spike, the density profile looks isochoric. The density spike in all three profiles scales with the average density. During the optimization, this density spike was created by a converging shock wave. The result is a density spike that tunes the maximum observed density over Euler's number to a value that is lower than the density in the plateau, but higher than the density before the shock. Thus, the outgoing shock wave is detected by the shell metric combined with the peak density set by the converging shock wave. This feature was useful for the metric but serves no purpose in a compression design. To avoid this coupling of the shell metric with the converging shock wave, we now resort to setting the boundary of the RMSE calculation at the position of the outgoing shock wave.

We construct a metric to find the outgoing shock wave at peak compression. A shock typically raises density and pressure over a short distance. In a first attempt, we multiplied the absolute inverted mass density scale length with the absolute inverted total pressure scale length and found the peak of that value. Using this metric on one of the optimized profiles from Fig. 5 detects the converged shock, which is not what we are looking for. To prevent this we multiply the cell mass onto the previous metric and test that metric with the swarm. The metric M_i for cell i is then defined by

$$M_i = \left| \frac{\log \rho_{i+1} - \log \rho_i}{r_{i+1} - r_i} \right| \cdot \left| \frac{\log P_{i+1} - \log P_i}{r_{i+1} - r_i} \right| \cdot (m_{i+1} + m_i), \tag{9}$$

with the pressure P_i (electron + ion pressure), the mass density ρ_i, and the mass m_i of the respective cells, where the units for all properties are arbitrary. This yields our next iteration of the objective function

$$O_4 = -\mathrm{RMSE}(\bar{\rho}, \mathrm{argmax}_i(M_i)) + w_{\mathrm{d}} \cdot \bar{\rho}, \tag{10}$$

where $\bar{\rho}$ is calculated over the same volume as the RMSE and all quantities are evaluated at the time of peak areal density. The compressed fuel mass density profile in Fig. 6 which was obtained by maximizing O_4 with $w_{\mathrm{d}} = 0.1$ is very flat around a density of 750 g/cm^3 except for a small $\sim 5\mu$m radius central hotspot. Around the time of peak compression the dynamics are dominated by two shock waves. One is traveling outwards and the other is reflected off the center.

Since there is a small central hotspot remaining, instead of using the cell mass weighted density error, we implemented a cell thickness d_n weighted error calculation

$$O_5 = -\mathrm{RMSE}_d(\bar{\rho}, \mathrm{argmax}_i(M_i)) + w_{\mathrm{d}} \cdot \bar{\rho}, \text{with} \tag{11}$$

$$\mathrm{RMSE}_d(\rho_{\mathrm{T}}, N) = \sqrt{\frac{\sum_{n=1}^{N} (\rho_n - \rho_{\mathrm{T}})^2 \cdot d_n}{\sum_n d_n}}. \tag{12}$$

This increases the relative importance of the center. We evaluate O_5 at the time of peak areal density as well. In Fig. 7, we present a very flat compressed fuel profile at a high density of over 600 g/cm^3 with a thickness of $\sim 25\,\mu$m along with the used temporal laser power profile. We used more particles (600) and more cycles (100) in the swarm compared to the previous optimizations. Although the average density is higher than the parameter range we aimed at, the achieved density is close enough to the required range. We can adjust the density with the density weight in future studies to achieve the desired values.

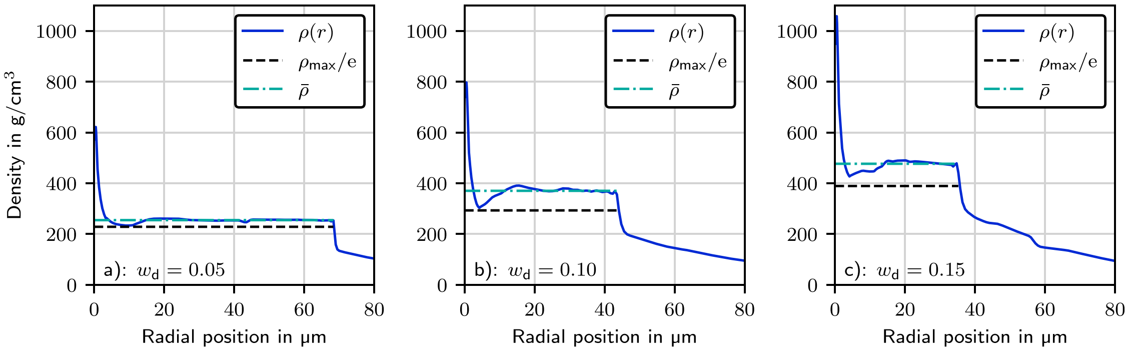

(I) Mass density profiles.

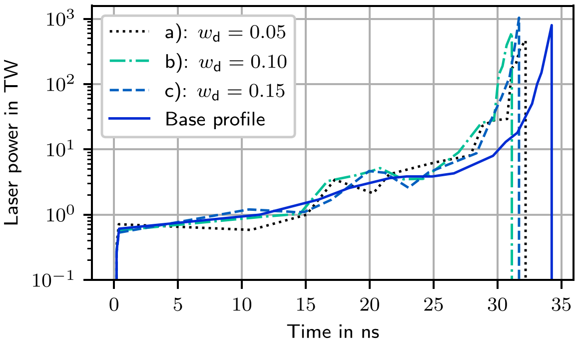

(II) Temporal laser power profiles.

FIG. 5. (I) shows the mass density vs radial position (blue line) at the time the O_3 objective function is maximized for the density weights (a): 0.05, (b): 0.10, and (c): 0.15 where the implosions achieved peak areal densities of 2.32 g/cm^2, 2.66 g/cm^2, and 2.91 g/cm^2, respectively. The black dashed line shows the maximum of the density divided by $\rho_{\mathrm{max}}/\mathrm{e}$, which marks the threshold for determining the outer radius for the calculation of the average density and the RMSE. The dashed dotted green line shows the average density. The temporal laser power profiles used in the optimized simulations can be found in (II) together with the base profile from Fig. 2.

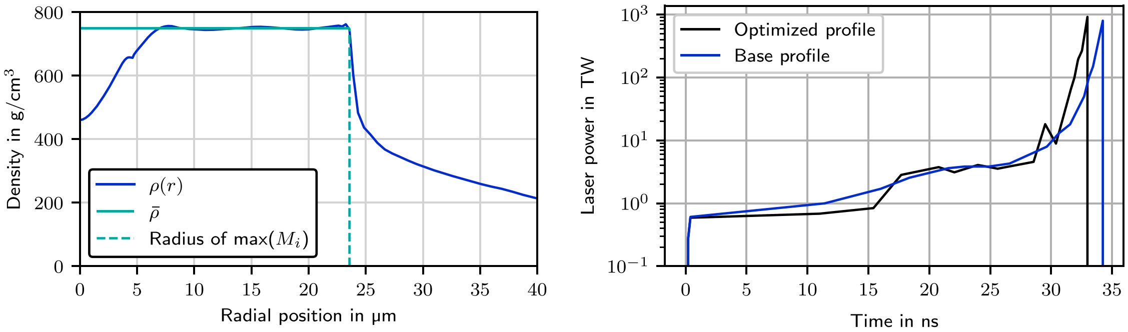

(I) Mass density profile.

(II) Temporal laser profile.

FIG. 6. The optimized mass density profile (I) with the shock detection metric and the objective function O_4 with $w_\mathrm{d} = 0.1$. The blue curve shows the profile at peak areal density (3.12 g/cm^2). The green line shows the average density and the dashed green line the radial position of the maximum of the shock detection metric, which is used as a boundary for the calculations. In (II) the temporal laser profile is shown together with the base profile from Fig. 2.

In Table I, we summarize the advantages and disadvantages of the objective functions. In future studies, the objective function can be modified to include constraints on metrics that indicate instability risks such as the in-flight-aspect-ratio or the laser intensity and the laser plasma density scale length. In our studies, we did not include the time evolution of the objective function which can also be used to estimate the length of the timing window when the ignitor should ignite the fuel and could be of benefit if the duration of that time window is too

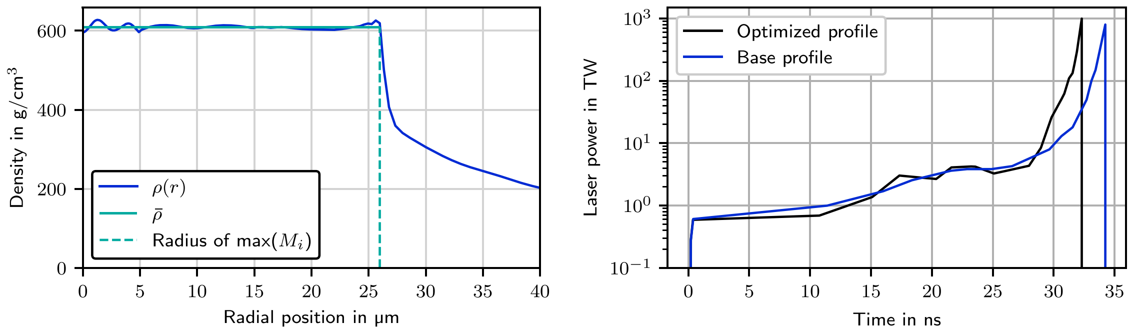

(I) Mass density profile.

(II) Temporal laser profile.

FIG. 7. The optimized mass density (I) and laser power (II) profiles with the objective function O_5 using $w_d = 0.1$. In (I) the blue curve shows the profile at peak areal density (2.90 g/cm^2). The temporal laser profile in (II) is drawn together with the base profile from Fig. 2.

TABLE I. Summary of the advantages and disadvantages of the studied objective functions.

Objective	Advantage	Disadvantage
O_1	Very high density	Small mass at high density
O_2	Partial compression of all DT	Density only achieved at center
O_3	Flat, thick, and tunable density profile	Density spike at center
O_4	Very flat high density profile	Dip at the center
O_5	Isochoric density profile	...

short. The objective function we used could also be applied to different gradient-less optimization techniques. In our problem sets, the particle swarm proved to reliably give the answers we requested with our objective functions. We did not have to adjust the hyperparameters for most of this study, which indicates a good robustness of the technique.

V. CONCLUSION

We applied particle swarm optimization to optimize inertial fusion energy target designs for the fast ignition approach. By combining the MULTI-IFE code with the particle swarm optimization technique, we achieved almost perfectly isochoric compression using the appropriate evaluation function. The key to this optimization is finding the appropriate objective function. We showed that an objective function that combines a thickness averaged root mean squared error from an average density with a reward for higher densities while determining the integration volume by an outgoing shock detection metric can attain a highly compressed isochoric fuel profile.

The presented simulations were not restricted in terms of the maximum laser power, and therefore, feature very high peak powers and intensities. Some of the shown simulations relied on very strong shocks toward the end of the pulse to achieve the void closure with ablation pressures sometimes exceeding 1Gbar. Furthermore, the found laser power profile requires a contrast ratio of the laser of the order of 1:1000 which for example exceeds stated power contrasts at the NIF (i.e., 1:50 in requirements[41] and 1:176 in shown experiments[42]) by more than a factor of 5. The small focal spot sizes used in the simulations would require a large numbers of beams to keep a good illumination uniformity. The central gas density of 10^{-6} g/cm^3 is very low and would require very low fielding temperatures of the target (about 11.3 K or more than 8 K below the triple point for DT[43]) We plan to use the shown method to tune temporal laser pulses for different targets and improve the experimental practicability of the design. In future runs we will also investigate the influence of substituting the 3ω-laser with a 2ω-laser while using a plastic ablator. We will assess the sensitivity of the isochoric compression designs to these changes and further explore the vast design space of fast ignition compression designs.

ACKNOWLEDGMENTS

Funding for this work was provided by Focused Energy GmbH. Special thanks to Dr. Markus Hesse for the calculation of the DT temperature for the low central gas density.

AUTHOR DECLARATIONS

Conflict of Interest

The authors have no conflicts to disclose.

Author Contributions

M. Brönner: Conceptualization (lead); Data curation (lead); Formal analysis (lead); Investigation (lead); Methodology (lead); Software (lead); Validation (equal); Visualization (lead); Writing – original draft (lead); Writing – review & editing (lead). **S. Atzeni:** Conceptualization (supporting); Supervision (equal); Validation (equal); Writing – review & editing (equal). **D. Callahan:** Conceptualization (equal); Methodology (equal); Resources (equal); Supervision (lead); Writing – review & editing (equal). **J. Gaffney:** Conceptualization (supporting); Methodology (supporting); Supervision (equal); Writing – review & editing (equal). **P. Gibbon:** Conceptualization (supporting); Methodology (supporting); Supervision (equal); Writing – review & editing (equal). **L. C. Jarrott:** Conceptualization (equal); Methodology (equal); Software (equal). **A. Mateo:** Methodology (supporting); Writing – review & editing (equal). **L. Savino:** Methodology (supporting); Validation (equal); Writing – review & editing (equal). **N. Schott:**

Conceptualization (equal); Methodology (equal); Writing – review & editing (equal). **W. Theobald:** Conceptualization (supporting); Resources (equal); Writing – review & editing (equal). **M. Roth:** Conceptualization (supporting); Funding acquisition (lead); Methodology (supporting); Resources (equal); Supervision (lead); Writing – review & editing (equal).

DATA AVAILABILITY

The data that support the findings of this study are available from the corresponding author upon reasonable request.

REFERENCES

[1] R. Ramis and J. Meyer-ter Vehn, Comput. Phys. Commun. **203**, 226 (2016).

[2] J. Kennedy and R. Eberhart, in *Proceedings of ICNN'95 - International Conference on Neural Networks* (IEEE, Perth, WA, Australia, 1995), Vol. 4, pp. 1942–1948.

[3] H. Abu-Shawareb, R. Acree, P. Adams, J. Adams, B. Addis, R. Aden, P. Adrian, B. B. Afeyan, M. Aggleton, L. Aghaian, A. Aguirre, D. Aikens, J. Akre, F. Albert, M. Albrecht *et al.*, Phys. Rev. Lett. **132**, 065102 (2024).

[4] A. B. Zylstra, O. A. Hurricane, D. A. Callahan, A. L. Kritcher, J. E. Ralph, H. F. Robey, J. S. Ross, C. V. Young, K. L. Baker, D. T. Casey, T. Döppner, L. Divol, M. Hohenberger, S. L. Pape, A. Pak, P. K. Patel, R. Tommasini, S. J. Ali, P. A. Amendt, L. J. Atherton, B. Bachmann, D. Bailey, L. R. Benedetti, L. Berzak Hopkins, R. Betti, S. D. Bhandarkar, J. Biener, R. M. Bionta, N. W. Birge, E. J. Bond, D. K. Bradley, T. Braun, T. M. Briggs, M. W. Bruhn, P. M. Celliers, B. Chang, T. Chapman, H. Chen, C. Choate, A. R. Christopherson, D. S. Clark, J. W. Crippen, E. L. Dewald, T. R. Dittrich, M. J. Edwards, W. A. Farmer, J. E. Field, D. Fittinghoff, J. Frenje, J. Gaffney, M. Gatu Johnson, S. H. Glenzer, G. P. Grim, S. Haan, K. D. Hahn, G. N. Hall, B. A. Hammel, J. Harte, E. Hartouni, J. E. Heebner, V. J. Hernandez, H. Herrmann, M. C. Herrmann, D. E. Hinkel, D. D. Ho, J. P. Holder, W. W. Hsing, H. Huang, K. D. Humbird, N. Izumi, L. C. Jarrott, J. Jeet, O. Jones, G. D. Kerbel, S. M. Kerr, S. F. Khan, J. Kilkenny, Y. Kim, H. Geppert Kleinrath, V. Geppert Kleinrath, C. Kong, J. M. Koning, J. J. Kroll, M. K. G. Kruse, B. Kustowski, O. L. Landen, S. Langer, D. Larson, N. C. Lemos, J. D. Lindl, T. Ma, M. J. MacDonald, B. J. MacGowan, A. J. Mackinnon, S. A. MacLaren, A. G. MacPhee, M. M. Marinak, D. A. Mariscal, E. V. Marley, L. Masse, K. Meaney, N. B. Meezan, P. A. Michel, M. Millot, J. L. Milovich, J. D. Moody, A. S. Moore, J. W. Morton, T. Murphy, K. Newman, J.-M. G. D. Nicola, A. Nikroo, R. Nora, M. V. Patel, L. J. Pelz, J. L. Peterson, Y. Ping, B. B. Pollock, M. Ratledge, N. G. Rice, H. Rinderknecht, M. Rosen, M. S. Rubery, J. D. Salmonson, J. Sater, S. Schiaffino, D. J. Schlossberg, M. B. Schneider, C. R. Schroeder, H. A. Scott, S. M. Sepke, K. Sequoia, M. W. Sherlock, S. Shin, V. A. Smalyuk, B. K. Spears, P. T. Springer, M. Stadermann, S. Stoupin, D. J. Strozzi, L. J. Suter, C. A. Thomas, R. P. J. Town, E. R. Tubman, C. Trosseille, P. L. Volegov, C. R. Weber, K. Widmann, C. Wild, C. H. Wilde, B. M. Van Wonterghem, D. T. Woods, B. N. Woodworth, M. Yamaguchi, S. T. Yang, and G. B. Zimmerman, Nature **601**, 542 (2022).

[5] A. L. Kritcher, A. B. Zylstra, C. R. Weber, O. A. Hurricane, D. A. Callahan, D. S. Clark, L. Divol, D. E. Hinkel, K. Humbird, O. Jones, J. D. Lindl, S. Maclaren, D. J. Strozzi, C. V. Young, A. Allen, B. Bachmann, K. L. Baker, T. Braun, G. Brunton, D. T. Casey, T. Chapman, C. Choate, E. Dewald, J.-M. G. Di Nicola, M. J. Edwards, S. Haan, T. Fehrenbach, M. Hohenberger, E. Kur, B. Kustowski, C. Kong, O. L. Landen, D. Larson, B. J. MacGowan, M. Marinak, M. Millot, A. Nikroo, R. Nora, A. Pak, P. K. Patel, J. E. Ralph, M. Ratledge, M. S. Rubery, D. J. Schlossberg, S. M. Sepke, M. Stadermann, T. I. Suratwala, R. Tommasini, R. Town, B. Woodworth, B. Van Wonterghem, and C. Wild, Phys. Rev. E **109**, 025204 (2024).

[6] M. M. Marinak, G. B. Zimmerman, T. Chapman, G. D. Kerbel, M. V. Patel, J. M. Koning, S. M. Sepke, B. Chang, C. R. Schroeder, J. A. Harte, D. S. Bailey, L. A. Taylor, S. H. Langer, M. A. Belyaev, D. S. Clark, J. Gaffney, B. A. Hammel, D. E. Hinkel, A. L. Kritcher, J. L. Milovich, H. F. Robey, and C. R. Weber, Phys. Plasmas **31**, 070501 (2024).

[7] S. Atzeni and J. Meyer-ter Vehn, *The Physics of Inertial Fusion: Beam Plasma Interaction, Hydrodynamics, Hot Dense Matter* (Clarendon Press, Oxford University Press, Oxford, New York, 2004).

[8] O. A. Hurricane, D. A. Callahan, P. T. Springer, M. J. Edwards, P. Patel, K. Baker, D. T. Casey, L. Divol, T. Döppner, D. E. Hinkel, L. F. Berzak Hopkins, A. Kritcher, S. Le Pape, S. Maclaren, L. Masse, A. Pak, L. Pickworth, J. Ralph, C. Thomas, A. Yian, and d A. Zylstra, Plasma Phys. Control. Fusion **61**, 014033 (2019).

[9] M. Tabak, J. Hammer, M. E. Glinsky, W. L. Kruer, S. C. Wilks, J. Woodworth, E. M. Campbell, M. D. Perry, and R. J. Mason, Phys. Plasmas **1**, 1626 (1994).

[10] R. Kodama, P. A. Norreys, K. Mima, A. E. Dangor, R. G. Evans, H. Fujita, Y. Kitagawa, K. Krushelnick, T. Miyakoshi, N. Miyanaga, T. Norimatsu, S. J. Rose, T. Shozaki, K. Shigemori, A. Sunahara, M. Tampo, K. A. Tanaka, Y. Toyama, T. Yamanaka, and M. Zepf, Nature **412**, 798 (2001).

[11] M. Roth, T. E. Cowan, M. H. Key, S. P. Hatchett, C. Brown, W. Fountain, J. Johnson, D. M. Pennington, R. A. Snavely, S. C. Wilks, K. Yasuike, H. Ruhl, F. Pegoraro, S. V. Bulanov, E. M. Campbell, M. D. Perry, and H. Powell, Phys. Rev. Lett. **86**, 436 (2001).

[12] B. M. Hegelich, B. J. Albright, J. Cobble, K. Flippo, S. Letzring, M. Paffett, H. Ruhl, J. Schreiber, R. K. Schulze, and J. C. Fernández, Nature **439**, 441 (2006).

[13] J. C. Fernández, J. Honrubia, B. J. Albright, K. A. Flippo, D. C. Gautier, B. M. Hegelich, M. J. Schmitt, M. Temporal, and L. Yin, Nucl. Fusion **49**, 065004 (2009).

[14] S. Atzeni, M. Temporal, and J. Honrubia, Nucl. Fusion **42**, L1 (2002).

[15] S. Atzeni, Phys. Plasmas **6**, 3316 (1999).

[16] S. Atzeni and M. Tabak, Plasma Phys. Control. Fusion **47**, B769 (2005).

[17] M. H. Key, Phys. Plasmas **14**, 055502 (2007).

[18] M. Tabak, D. S. Clark, S. P. Hatchett, M. H. Key, B. F. Lasinski, R. A. Snavely, S. C. Wilks, R. P. J. Town, R. Stephens, E. M. Campbell, R. Kodama, K. Mima, K. A. Tanaka, S. Atzeni, and R. Freeman, Phys. Plasmas **12**, 057305 (2005).

[19] J. Fernández, B. Albright, F. Beg, M. Foord, B. Hegelich, J. Honrubia, M. Roth, R. Stephens, and L. Yin, Nucl. Fusion **54**, 054006 (2014).

[20] L. C. Jarrott, M. S. Wei, C. McGuffey, A. A. Solodov, W. Theobald, B. Qiao, C. Stoeckl, R. Betti, H. Chen, J. Delettrez, T. Döppner, E. M. Giraldez, V. Y. Glebov, H. Habara, T. Iwawaki, M. H. Key, R. W. Luo, F. J. Marshall, H. S. McLean, C. Mileham, P. K. Patel, J. J. Santos, H. Sawada, R. B. Stephens, T. Yabuuchi, and F. N. Beg, Nat. Phys. **12**, 499 (2016).

[21] J. Zhang, W. M. Wang, X. H. Yang, D. Wu, Y. Y. Ma, J. L. Jiao, Z. Zhang, F. Y. Wu, X. H. Yuan, Y. T. Li, and J. Q. Zhu, Phil. Trans. R. Soc. A **378**, 20200015 (2020).

[22] C. McGuffey, J. Kim, M. S. Wei, P. M. Nilson, S. N. Chen, J. Fuchs, P. Fitzsimmons, M. E. Foord, D. Mariscal, H. S. McLean, P. K. Patel, R. B. Stephens, and F. N. Beg, Sci. Rep. **10**, 9415 (2020).

[23] A. J. Kemp, S. C. Wilks, and M. Tabak, Phys. Plasmas **31**, 042709 (2024).

[24] J. J. Honrubia, J. C. Fernández, M. Temporal, B. M. Hegelich, and J. Meyer-ter Vehn, J. Phys.: Conf. Ser. **244**, 022038 (2010).

[25] J. J. Honrubia, J. C. Fernandez, M. Temporal, B. M. Hegelich, and J. Meyer-ter Vehn, Phys. Plasmas **16**, 102701 (2009).

[26] J. J. Honrubia and M. Murakami, Phys. Plasmas **22**, 012703 (2015).

[27] H. D. Shay, P. Amendt, D. Clark, D. Ho, M. Key, J. Koning, M. Marinak, D. Strozzi, and M. Tabak, Phys. Plasmas **19**, 092706 (2012).

[28] V. N. Goncharov, T. C. Sangster, R. Betti, T. R. Boehly, M. J. Bonino, T. J. B. Collins, R. S. Craxton, J. A. Delettrez, D. H. Edgell, R. Epstein, R. K. Follett, C. J. Forrest, D. H. Froula, V. Yu. Glebov, D. R. Harding, R. J. Henchen, S. X. Hu, I. V. Igumenshchev, R. Janezic, J. H. Kelly, T. J. Kessler, T. Z. Kosc, S. J. Loucks, J. A. Marozas, F. J. Marshall, A. V. Maximov, R. L. McCrory, P. W. McKenty, D. D. Meyerhofer, D. T. Michel, J. F. Myatt, R. Nora, P. B. Radha, S. P. Regan, W. Seka, W. T. Shmayda, R. W. Short, A. Shvydky, S. Skupsky, C. Stoeckl, B. Yaakobi, J. A. Frenje, M. Gatu-Johnson, R. D. Petrasso, and D. T. Casey, Phys. Plasmas **21**, 056315 (2014).

[29] D. Clark and M. Tabak, Nucl. Fusion **47**, 1147 (2007).

[30] R. Poli, J. Kennedy, and T. Blackwell, Swarm Intell. **1**, 33 (2007).

[31] A. G. Gad, Arch. Comput. Methods Eng. **29**, 2531 (2022).

[32] M. Clerc and J. Kennedy, IEEE Trans. Evol. Comput. **6**, 58 (2002).

[33] R. Albers and J. Johnson, "SESAME 5271," in Report No. LA-UR-92-3407 (Los Alamos National Laboratory, 1995).

[34] B. M. Haines, J. P. Sauppe, P. A. Keiter, E. N. Loomis, T. Morrow, D. S. Montgomery, L. Kuettner, B. M. Patterson, T. E. Quintana, J. Field, M. Millot, P. Celliers, D. C. Wilson, H. F. Robey, R. F. Sacks, D. J. Stark, C. Krauland, and M. Rubery, Phys. Plasmas **28**, 032709 (2021).

[35] S. Atzeni, Comput. Phys. Commun. **43**, 107 (1986).

[36] S. Atzeni, A. Schiavi, F. Califano, F. Cattani, F. Cornolti, D. Del Sarto, T. Liseykina, A. Macchi, and F. Pegoraro, Comput. Phys. Commun. **169**, 153 (2005).

[37] S. Atzeni, A. Caruso, and V. Pais, Laser Part. Beams **4**, 393 (1986).

[38] K. Eidmann, Laser Part. Beams **12**, 223 (1994).

[39] S. Atzeni, A. Schiavi, J. J. Honrubia, X. Ribeyre, G. Schurtz, P. Nicolaï, M. Olazabal-Loumé, C. Bellei, R. G. Evans, and J. R. Davies, Phys. Plasmas **15**, 056311 (2008).

[40] J. Lindl, Phys. Plasmas **2**, 3933 (1995).

[41] J. Paisner, J. D. Boyes, S. A. Kumpan, W. H. Lowdermilk, and M. S. Sorem, in *Solid State Lasers for Application to Inertial Confinement Fusion (ICF)* (SPIE, 1995), Vol. 2633, pp. 2–12.

[42] C. A. Haynam, P. J. Wegner, J. M. Auerbach, M. W. Bowers, S. N. Dixit, G. V. Erbert, G. M. Heestand, M. A. Henesian, M. R. Hermann, K. S. Jancaitis, K. R. Manes, C. D. Marshall, N. C. Mehta, J. Menapace, E. Moses, J. R. Murray, M. C. Nostrand, C. D. Orth, R. Patterson, R. A. Sacks, M. J. Shaw, M. Spaeth, S. B. Sutton, W. H. Williams, C. C. Widmayer, R. K. White, S. T. Yang, and B. M. Van Wonterghem, Appl. Opt. **46**, 3276 (2007).

[43] P. Souers, "Cryogenic hydrogen data pertinent to magnetic fusion energy," Tech. Rep. UCRL-52628, 6205719 (Lawrence Livermore National Lab. (LLNL), Livermore, CA, 1979).